# Analyzing Aircraft Controllability After Engine Failure During Takeoff in Adverse Weather Conditions

Koolstra, Herman; Huijbrechts, Erik-Jan; Mulder, Bob

**DOI**
10.2514/1.C035219

**Publication date**
2019

**Document Version**
Final published version

**Published in**
Journal of Aircraft: devoted to aeronautical science and technology

**Citation (APA)**
Koolstra, H., Huijbrechts, E.-J., & Mulder, B. (2019). Analyzing Aircraft Controllability After Engine Failure During Takeoff in Adverse Weather Conditions. *Journal of Aircraft: devoted to aeronautical science and technology*, *56*(4), 1330-1341. https://doi.org/10.2514/1.C035219

# Analyzing Aircraft Controllability After Engine Failure During Takeoff in Adverse Weather Conditions

Herman J. Koolstra,* Erik-Jan Huijbrechts,† and J. A. Mulder‡
*Delft University of Technology, 2600 GB Delft, The Netherlands*

DOI: 10.2514/1.C035219

**When an aircraft experiences an engine failure during takeoff, it must be able to either reject or continue the takeoff without exceeding the longitudinal or lateral dimensions of the usable runway. This paper focuses on the lateral deviation. During certification, the minimum control speed ground is determined in certification tests; at this speed, the allowable maximum lateral deviation is 30 ft. These tests are done with a free castering nose wheel and other requirements such as not using ailerons. These are all $V_{mcg}$ increasing factors. On the other hand, the aircraft manufacturer chooses the most favorable conditions, new tires, a dry runway, and no crosswind. It is unclear if the free castering nose wheel is a stringent-enough requirement to compensate for reduced runway friction, and the effect of crosswind is not considered in the certification tests. Furthermore, the rejected takeoff condition is not certified against a lateral excursion limit. Therefore, in this paper, a model is developed to determine the lateral deviation in a continued as well as a rejected takeoff, including the effect of pilot reaction time, runway surface condition, and crosswind. For the present evaluation, a Boeing 737-300 model was used.**



## Nomenclature

| | | |
|---|---|---|
| $b$ | = | wingspan, m |
| $C_D$ | = | drag coefficient |
| $C_L$ | = | lift coefficient |
| $C_l$ | = | roll moment coefficient |
| $C_n$ | = | yaw moment coefficient |
| $C_Y$ | = | side force coefficient |
| $D$ | = | drag, N |
| $F$ | = | force, N |
| $g$ | = | acceleration due to gravity, m/s$^2$ |
| $I_{zz}$ | = | inertia moment around body $Z$ axis, kg · m$^2$ |
| $K_{zz}$ | = | nondimensional inertia moment around the $Z$ axis |
| $L$ | = | lift, N |
| $M$ | = | moment, N · m |
| $m$ | = | aircraft mass, kg |
| $N1$ | = | engine fan rotation frequency, rpm |
| $q$ | = | dynamic pressure $(1/2)\rho V^2$, N/m$^2$ |
| $R_c$ | = | runway surface condition |
| $r$ | = | yaw rate, rad/s |
| $r_{no}$ | = | displacement vector (where "no" is a number), m |
| $r_{y,eng}$ | = | distance of engine thrust line to c.g. in the body $Y$-axis direction, m |
| $S$ | = | wing area, m$^2$ |
| $T$ | = | thrust, N |
| $u$ | = | inertial velocity in body $x$ direction, m/s |
| $V$ | = | velocity relative to the air, m/s |
| $V_g$ | = | inertial velocity relative to the ground, m/s |
| $V_{mca}$ | = | minimum control speed air, kt |
| $V_{mcg}$ | = | minimum control speed ground, kt |
| $v$ | = | inertial velocity in body $y$ direction, m/s |
| $W_b$ | = | wheel base parameter, m |
| $X_b$ | = | $X$ axis of the aircraft in body reference frame |
| $X_g$ | = | $X$ axis in the local-level reference frame (coincides with runway centerline) |
| $X_{wnd}$ | = | crosswind in the local-level reference frame, m/s |
| $Y_b$ | = | $Y$ axis of the aircraft in body reference frame |
| $Y_g$ | = | $Y$ axis in the local-level reference frame |
| $Z_b$ | = | $Z$ axis of the aircraft in body reference frame, in the plane of symmetry pointing down |
| $Z_g$ | = | $Z$ axis in the local-level reference frame, pointing straight down |
| $\beta$ | = | aerodynamic sideslip angle, rad |
| $\beta_g$ | = | tire sideslip angle, rad |
| $\delta_{nw}$ | = | nose wheel deflection, rad |
| $\delta_r$ | = | rudder deflection, rad |
| $\delta_t$ | = | throttle input |
| $\kappa$ | = | track angle relative to the ground, rad |
| $\mu$ | = | friction coefficient |
| $\mu_s$ | = | side force friction coefficient |
| $\rho$ | = | air density, kg/m$^3$ |
| $\psi$ | = | heading, rad |

*Subscripts*

| | | |
|---|---|---|
| aero | = | aerodynamic |
| $b$ | = | relative to body or in body coordinate system |
| cg | = | center of gravity |
| eng | = | engine |
| $g$ | = | relative to the ground or in local-level coordinate system |
| gear | = | related to the undercarriage |
| left | = | self-explanatory |
| max | = | maximum |
| mw | = | main wheel, s |
| nw | = | nose wheel |
| $n$ | = | around the $Z_b$ axis |
| nws | = | nose wheel steering |
| req | = | required |
| right | = | self-explanatory |
| wnd | = | wind |
| $x$ | = | in $x$ direction in body or local-level frame |
| $y$ | = | in $y$ direction in body or local-level frame |
| $z$ | = | in $z$ direction in body or local-level frame |

Received 20 August 2018; revision received 27 November 2018; accepted for publication 28 November 2018; published online 24 January 2019. 

*Experimental Test Pilot, Faculty of Aerospace Engineering, Control and Simulation Division.

†Captain Boeing 737, KLM Royal Dutch Airlines, Amstelveen.

‡Professor, Faculty of Aerospace Engineering, Control and Simulation Division, P.O. Box 5058; J.A.Mulder@tudelft.nl.

## I. Introduction

THERE are hardly any quantitative data publicly available on the effect of engine failure on lateral deviation. One source is the quantitative data available from $V_{mcg}$ testing, but the usability of these data is limited because all these tests are performed under

specific conditions. The certification authorities require a free castering nose wheel, the most adverse aircraft mass with the most aft c.g. Additional requirements are that the pilot must react on outside references only and not use aileron. These requirements are unfavorable and will increase $V_{\mathrm{mcg}}$. During the certification test, the aircraft manufacturer will set all the remaining parameters as optimal as possible: a fast (but within limits) reaction time of the test pilot, new tires, a dry runway, and no crosswind. Therefore, $V_{\mathrm{mcg}}$ test results apply only to these conditions, and data on how runway surface condition, crosswind, and reaction time will affect the lateral deviation are not publicly available.

Although $V_{\mathrm{mcg}}$ is only applicable for one specific situation, all full-flight simulators have the options for rejected and continued takeoff in adverse weather conditions. However, the authors have experienced that, when rejected or continued takeoff under adverse weather conditions was practiced in different simulators, the amount of lateral deviation after an engine failure could differ significantly between simulators. Some simulators only showed a lateral deviation of a few feet when the engine was failed close to $V_{\mathrm{mcg}}$ speed even on slippery runways. It should also be noted that there are no requirements to include data of rejected or continued takeoff under adverse weather conditions in the qualitative test guide (QTG) used for simulator qualification; this might be a direct result of the fact that those data are not available because these tests are not required for aircraft certification. Obviously, the aerodynamic models must be accurate, otherwise the simulator would not have passed QTG qualification, but it questions the validity of the ground models used in simulators.

It is not the intent of this paper to change the present aircraft certification procedure. There are two reasons for this approach. First, procedures to change certification are quite slow and cumbersome, and second, it will only affect new aircraft because older aircraft will have grandfather rights. Our approach is to show that, for all aircraft, an engineering analysis can be made based on the combination of the aircraft's data, an agreed ground surface model, and a simplified pilot model.

Furthermore, when we can estimate the effect of adverse weather conditions on aircraft controllability during rejected and continued takeoff, it is also possible to adjust takeoff figures, in particular $V1$, for these effects. In this paper, the model is derived. Our model combines the aerodynamic and geometric properties of a Boeing 737-300 with a tire friction model derived from NASA tire characteristic measurements [1]. This model was evaluated by simulating the $V_{\mathrm{mcg}}$ certification test and proved to be representative by accurately reproducing the certified $V_{\mathrm{mcg}}$ value. With this model, we could simulate the effect of pilot reaction time, runway surface condition, and crosswind on aircraft lateral deviation. The simulations involved scenarios with continued as well as rejected takeoff.



## II. Model Design

### A. General

The authors did not have access to the official aircraft data from the aircraft manufacturer. Therefore, a different road was traveled. Most aircraft data were retrieved using the DATCOM plus program.[§] Other data were gathered from the aircraft flight manual, from the flight crew operations manual (FCOM), and by reverse engineering using $V_{\mathrm{mca}}$. This gave us a generic Boeing 737-300 model. To compensate for the lack of genuine aerodynamic aircraft parameters, we included a parameter sensitivity test. With this test, we evaluated how a (relatively large) change in a model parameter would affect the $V_{\mathrm{mcg}}$ and how this change would affect the change of $V_{\mathrm{mcg}}$ with crosswind and changed runway surface conditions. This evaluation will show that not all parameters are critical, and it confirmed that our model is usable for assessing the effect of crosswind and different runway surface conditions.

A special concern was the availability of side force coefficients $\mu_s$ for aircraft tires under various runway surface conditions. Most data were only applicable at low speed. The only open source found on $\mu_s$ at relatively high speed (100 kt) was the NASA paper [1] from 1977. A limitation of this report is the fact that it only covers concrete runways and only three types of surface conditions (dry, damp, and flooded), even though it would have been interesting to have more types of runway surfaces available, such as grooved pavement and ice patches. Furthermore, the author's experience[¶] is that wet concrete runways are far more slippery than, for example, wet asphalt-covered runways. Therefore, it would have been beneficial to have data for different types of runway surfaces. To compensate for this lack of data, the option of a speed-independent $\mu_s$ was incorporated. This makes it possible to calculate the effect of the changed $\mu_s$, but without the possibility to link this to a specific runway type, runway surface condition, and speed. This gives, for example, the option to calculate the lateral deviation at very low or even zero friction values. This can be used to find a (laterally) safe V1 speed, for very slippery runway surface conditions.

We will first cover the used reference frames and coordinate systems, and then we will discuss the different submodels used in our simulation. Subsequently, we will discuss the influence of time delays, runway surface condition, and crosswind on the continued takeoff. Next, we discuss the changes applied to model at rejected takeoff. Finally, we show the results of the sensitivity test and present our conclusion.

In this paper, we will not discuss how the results can be used by aircraft operators. This is discussed in a separate paper [2].

### B. Reference Frames

Because our simulations are of short duration and at relatively low speed, the effect of Earth rotation and curvature can be disregarded, which enables us to use the runway as our inertial frame, and we will use the subscript $g$ to denote this frame. The $X_g$ axis is aligned with the runway centerline, and the $Y_g$ axis is to the right in the surface plane. The origin of the frame is located at the start point of the takeoff roll. The second frame used is the aircraft body frame, for which we use the subscript $b$. Both frames are depicted in Fig. 1a. In our simulation, the $X_b$ axis remains in the plane parallel to the runway, and the aircraft does not roll; consequently, lift and drag can be expressed directly in the body axis, and the transformation between the two coordinate systems requires only a rotation around the $Z$ axis, which is pointing vertically down, over the heading $\psi$.

In Fig. 1b, the used velocities are depicted. The inertial velocity in the $X_b$ direction is $u$ and in the $Y_b$ direction is $v$. Consequently, the slip angle over the ground is $\beta_g = \arctan(v/u)$; similar to the aerodynamic sideslip, $\beta_g$ is positive if the ground track vector $V_g$ is to the right of the heading vector $u$. The inertial velocity is $V_g = \sqrt{(u^2 + v^2)}$. The track is depicted by the symbol $\kappa = \psi + \beta_g$, and to calculate the velocities in the inertial frame, we use $V_{g,x} = V_g \cos(\kappa)$ and $V_{g,y} = V_g \sin(\kappa)$.

The aerodynamic sideslip $\beta$ is derived by expressing the opposite of the wind vector in body axis coordinates and adding these to $u$ and $v$. As depicted in Fig. 2a, $\beta$ is

$$\beta = \arctan\left(\frac{v + V_{y,\mathrm{wnd}}}{u + V_{x,\mathrm{wnd}}}\right) \tag{1}$$

Because we only use right crosswind (which is positive), we get $V_{x,\mathrm{wnd}} = X_{\mathrm{wnd}} \sin(\psi)$ and $V_{y,\mathrm{wnd}} = X_{\mathrm{wnd}} \cos(\psi)$.

[§]Datcom is the U.S. Air Force Data Compendium, a 3100-page collection of the equations used in design of airplanes. This manual dates back to the 1930–1950s, before computers, when designs and calculations were done by hand and with slide rules. Digital Datcom is the computer program written in the 1960–1970s to incorporate many of these techniques into a computer program, to speed the process of analyzing a new or existing aircraft design.

[¶]The author was a member of the team that investigated a lateral runway excursion of a Royal Netherlands Air Force F16 in the 1990s. It was proven that the crosswind effect of the dragchute combined with the very rough open asphalt structure caused an uncontrollable yaw into the wind at lower speeds that caused the aircraft to depart the runway at the upwind side. However, in the simulator, the aircraft drifted in the opposite direction.

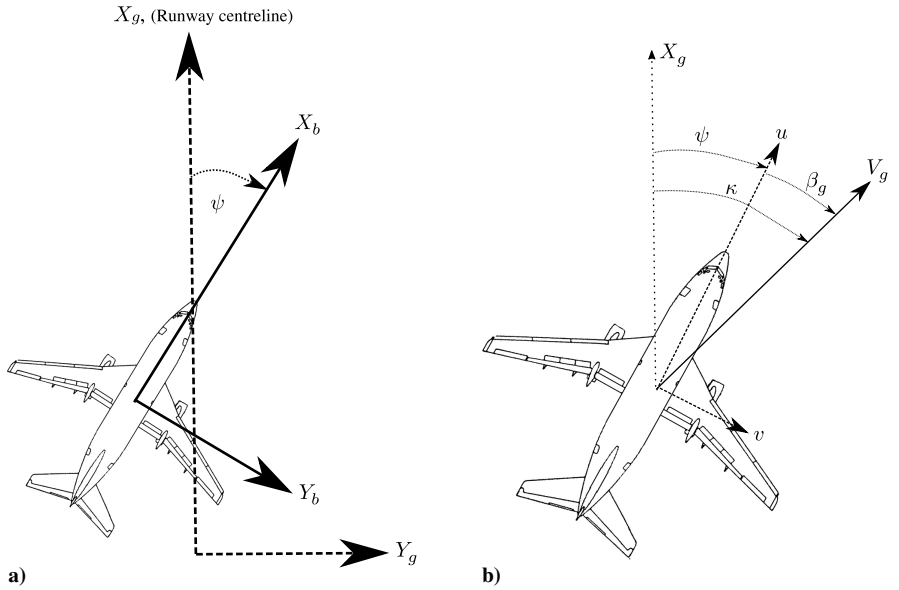


**Fig. 1 Representations of a) used reference frames, and b) used speeds and angles.**

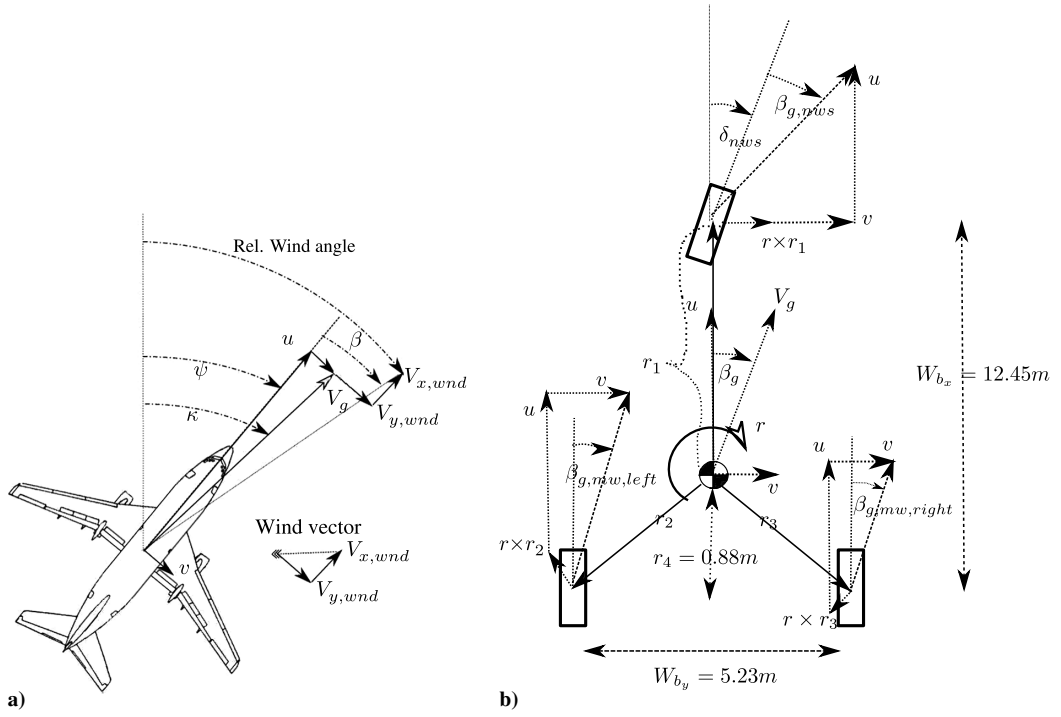


**Fig. 2 Representations of a) ground slip angle and aerodynamic slip angle, and b) slip angle corrections needed for the yaw rate *r*.**

Previously, we determined the slip angle with the ground ($\beta_g$); this represents the slip angle at the center of gravity. Because of the yaw rate $r$, the actual slip angle at each wheel is different. For each wheel position, we have to add the speed components in the $X_b$ and $Y_b$ directions caused by the yaw rate, as shown in Fig. 2b.

For the left and right main wheels, the slip angles become

$$\beta_{g,\text{mw,left}} = \arctan\left(\frac{v - r.r_4}{u + r.(W_{b_y}/2)}\right),$$
$$\text{and } \beta_{g,\text{mw,right}} = \arctan\left(\frac{v - r.r_4}{u - r.(W_{b_y}/2)}\right) \tag{2}$$

For the nose wheel slip angle, we also have to add the nose wheel deflection (for nose wheel deflection, we used the same rule as for rudder deflection: deflection to the left is positive). This gives

$$\beta_{g,\text{nw}} = \delta_{\text{nw}} + \arctan\left(\frac{v + r.|r_1|}{u}\right) \tag{3}$$

where $|r_1|$ is the length of the vector $r_1$. To calculate $|r_1|$ and $r_4$, the Boeing 737 technical publications [3] were used; these data are shown in Table 1. The lengths of $r_1$ and $r_4$ are dependent on the location of the c.g. For the determination of $V_{\text{mcg}}$, the lowest weight with the most aft c.g. is used, and we use the same configuration for our simulations. Based on the FCOM for the Boeing 737-300 [4], this is an aircraft weight of 40 tons with the c.g. at 28% mean aerodynamic chord (MAC). Using the data from Table 1, we derive that $r_4 =$ 0.88 m and $|r_1| = 11.57$ m.

**Table 1 Gear parameters**

| Parameter | Distance from datum (or length), m |
|---|---|
| Begin MAC | 15.89 |
| Main gear | 17.73 |
| Nose gear | 5.28 |
| Center of gravity at 28% MAC | 16.85 |
| MAC | 3.446 |
| $W_{b_x}$ | 12.45 |
| $W_{b_y}$ | 5.23 |
| $W_{b_z}$ | 2.89 |

### C. Aerodynamic and Engine Forces and Moments

The data used for the calculation of the aerodynamic forces, moments, and linear and rotational accelerations are presented in Table 2. For the values of wing surface area $S$, wingspan $b$, and engine thrust $T$, Boeing data were available [4]. For mass and c.g., the FCOM data were used. For the calculation of the inertia moment around the $Z$ axis, we used the rule [5] that the nondimensional radius of gyration ($K_{zz}$) for these types of aircraft is typically 0.037. This will give an inertia moment around the $Z$ axis of $I_{zz} = K_{zz}mb^2$.

Most other aerodynamic coefficients were derived using the DATCOM plus program. The coefficients $Cn_{\delta_r}$ and $Cy_{\delta_r}$ were estimated from the $V_{\text{mca}}$ speed of 105 kt for the Boeing 737-300 with 98 kN engines [4]. In this derivation, it was assumed that $\beta$ at $V_{\text{mca}}$ speed was zero, and consequently the engine moment was corrected by the rudder alone. For the calculation of $C_{Y_{\delta_r}}$ from $C_{n_{\delta_r}}$, we estimated, based on the drawings of the Boeing 737-300, that the rudder arm in relation to the c.g. was 14.82 m. In a similar way, the coefficient $C_{l_{\delta r}}$ was derived from $C_{Y_{\delta_r}}$ based on the measurement that this rudder acts 5.3 m above the c.g.

For the engine model, a speed independent thrust of 88.9 kN is used, and from the aircraft drawings, the engine arm $r_{y,\text{eng}}$ is estimated. The lift and drag coefficients depend on the flap setting used for takeoff. The values we use are the estimated values for 5 deg flap. The used coefficients and values are depicted in Table 2.

For the engine moment around the $Y_b$ axis, we estimated that the engine thrust line is 1 m below the c.g. We also assumed that the aircraft is trimmed for takeoff and that the pitch moments due to $C_{m_\alpha}$, $C_{m_{\delta ht}}$, and $C_{m_{\delta e}}$ cancel each other.

For the aerodynamic, thrust, and weight forces and moments, we use the subscript "aero" to differentiate these forces and moments from the forces and moments on the undercarriage, for which we use the subscript "gear". The subscript "gear" is only used for the total force or moments on all the wheels of the undercarriage. For forces and moments on the main wheels and nose wheel, we use the subscripts "mw" and "nw", respectively. For the calculation of the forces and moments, we limit the number of coefficients to the derivatives to $\beta$, $\delta_r$, and $r$. The angle of attack is assumed to be constant, giving a constant $C_L$ and $C_D$ value. Because freedom of movement in roll and pitch is very limited, no derivatives to $p$ and $q$ are required:

**Table 2 Aerodynamic parameters used**

| Parameter | Value |
|---|---|
| $S$ | 105.4 m$^2$ |
| $b$ | 28.88 m |
| $T$ (per engine) | 88.9 kN |
| $r_{y,\text{eng}}$ | 4.83 m |
| $I_{zz}$ | $1.2344 \times 10^6$ kg $\cdot$ m$^2$ |
| $\delta_{r,\max}$ | 26 deg |
| $\delta_{\text{nw,max}}$ | 7 deg |
| $C_{l_\beta}$ | −0.141 |
| $C_{l_{\delta r}}$ | −0.059 |
| $C_{l_r}$ | 0.141 |
| $C_{Y_\beta}$ | −0.96 |
| $C_{Y_{\delta r}}$ | 0.37 |
| $C_{n_\beta}$ | 0.18 |
| $C_{n_{\delta r}}$ | −0.19 |
| $C_{n_r}$ | −0.28 |
| $C_L$ | 0.477 |
| $C_D$ | 0.076 |

$$F_{x,\text{aero}} = T_{\text{left}} + T_{\text{right}} - qSC_d \tag{4}$$

$$F_{y,\text{aero}} = qS(C_{y_\beta} \cdot \beta + C_{y_{\delta_r}} \cdot \delta_r) \tag{5}$$

$$F_{z,\text{aero}} = mg - qSC_L \tag{6}$$

$$M_{z,\text{aero}} = qSb\left(C_{n_\beta} \cdot \beta + C_{n_{\delta r}} \cdot \delta_r + C_{n_r} \cdot \frac{rb}{2\,\text{V}}\right) + T_{\text{left}} \cdot |r_{y,\text{eng}}| - T_{\text{right}} \cdot |r_{y,\text{eng}}| \tag{7}$$

For the roll moment, we assume that there is no pilot aileron input:

$$M_{x,\text{aero}} = qSb\left(C_{l_\beta} \cdot \beta + C_{l_{\delta r}} \cdot \delta_r + C_{l_r} \cdot \frac{rb}{2\,\text{V}}\right) \tag{8}$$

Because the moments of $C_m$ and $C_{\delta e}$ are assumed to cancel each other, only the thrust remains with an arm of 1.0 m:

$$M_{y,\text{aero}} = 1.0(T_{\text{left}} + T_{\text{right}}) \tag{9}$$

### D. Gear Submodel

The friction forces between tire and runway are dependent on the normal force on the tire and the runway friction coefficients. The normal loads on the main wheels and nose wheel must balance the moments around the $Y_b$ and $X_b$ axes and carry the weight of the aircraft minus its lift. In matrix form, this gives

$$0 = \begin{bmatrix} M_{x,\text{aero}} + M_{x,\text{gear}} \\ M_{y,\text{aero}} + M_{y,\text{gear}} \\ \text{mg-Lift} \end{bmatrix} + \begin{bmatrix} 0 & -0.5W_b & 0.5W_b \\ -|r_1| & r_4 & r_4 \\ 1 & 1 & 1 \end{bmatrix} \begin{bmatrix} F_{z,\text{nw}} \\ F_{z,\text{mw,left}} \\ F_{z,\text{mw,right}} \end{bmatrix} \tag{10}$$

Solving this matrix gives the three normal forces. The side force on the tires ($F_{y,\text{gear}}$) is calculated by multiplying the normal load with the side force coefficient $\mu_s$. This side force coefficient is dependent on runway surface condition $R_c$, and slip angle and ground velocity and will be discussed in the section on the runway friction model.

The forces in the $X_b$ direction ($F_{x,\text{gear}}$) depend on the braking mode. Without braking, only rolling friction is assumed with $\mu_{\text{roll}} = 0.015$. When the brakes are used, the braking friction $\mu_d$ is also determined using the NASA model.

If nose wheel steering is not used, it is assumed that the nose wheel is free castering, and no side forces are generated by the nose wheel. When nose wheel steering is engaged, it is coupled with the rudder, and the ratio between rudder deflection and nose wheel steering is 26/7.

This gives the following friction forces on the gear:

$$F_{x,\text{gear}} = F_{z,\text{nw}}\mu_{\text{roll}} + F_{z,\text{mw,left}}\mu_{\text{roll}} + F_{z,\text{mw,right}}\mu_{\text{roll}} \tag{11}$$

$$F_{y,\text{gear}} = F_{z,\text{nw}}\mu_{s,\text{nw}}\text{sign}(\beta_{g,\text{nw}}) + F_{z,\text{mw,left}}\mu_{s,\text{mw,left}}\text{sign}(\beta_{g,\text{mw,left}}) + F_{z,\text{mw,right}}\mu_{s,\text{mw,right}}\text{sign}(\beta_{g,\text{mw,right}}) \tag{12}$$

where $\mu_{\text{roll}}$ in the first row must be replaced by $\mu_d$ if brakes are applied on that wheel. Because the normal force is always negative and $\mu_s$ is always positive, we need the sign() function in the second row so that a negative slip angle gives a positive side force.

The gear moments are derived by multiplying the gear friction forces with their respective arms as given in Fig. 2b and Table 1:

$$M_{x,\text{gear}} = -W_{b_z}(F_{y,\text{mw,left}} + F_{y,\text{mw,right}} + F_{y,\text{nw}}) \tag{13}$$

$$M_{y,\text{gear}} = -W_{b_z}(F_{x,\text{nw}} + F_{x,\text{mw,left}} + F_{x,\text{mw,right}}) \tag{14}$$

$$M_{z,\text{gear}} = -(F_{y,\text{mw,left}} + F_{y,\text{mw,right}})r_4 + F_{y,\text{nw}}r_1 + F_{x,\text{mw,left}}\frac{W_{b_y}}{2} - F_{x,\text{mw,rigt}}\frac{W_{b_y}}{2} \tag{15}$$

### E. Dynamic Submodel

For the forces and moments, we have used a full three-dimensional model to account for the asymmetric forces on the landing gear. However, we also assume the landing gear to be stiff; hence, $\dot{w}$, $\dot{p}$, and $\dot{q}$ are zero. This reduces the dynamic model to three equations. The simulation is done with a 0.01 s time step using the Euler integration method. The equations used are depicted next:

$$\dot{u} = (F_{x,\text{aero}} + F_{x,\text{gear}})/m + rv - qw \tag{16}$$

$$\dot{v} = (F_{y,\text{aero}} + F_{y,\text{gear}})/m - ru + pw \tag{17}$$

Because of the reduced degrees of freedom, the tangent acceleration terms in Eqs. (16) and (17) related to roll $pw$ and pitch $-qw$ are zero and can therefore be omitted. Because there is only rotation around the $Z_b$ axis, the terms related to the vector product of the angular velocity and the angular moment ($\omega \times I\omega$) are zero, and the rotational acceleration simplifies to Eq. (18). Integrating twice will give the heading $\psi$:

$$\dot{r} = (M_{z,\text{aero}} + M_{z,\text{gear}})/I_{zz} \tag{18}$$

### F. Runway Friction Submodel

To discuss runway friction, we need two different $\mu$ values. These are defined by the authors of [1] as follows.

1) $\mu_{d,\max}$ is the ratio between the normal force on the tire and the maximum braking force using the optimum slip.

2) $\mu_s$ is the ratio between the normal force on the tire and the side force. This $\mu_s$ depends on the slip angle, runway surface condition, and ground speed, and we need to model this $\mu_s$ to calculate the side forces on the gear.

NASA [1] shows that all $\mu$ values depend not only on the runway surface condition but also on the speed. Based on the NASA paper, models were created to be used in our simulation. The NASA paper distinguishes three types of runways: dry, damp, and flooded. The tabular data of the report were used to derive three models for these three different runway surface conditions. For the relation with the slip angle, we simplified Pacejka's magic formula [6] to an arctangent relationship. For the relation between velocity and $\mu_s$, an exponential relationship is used. The following runway friction models were established:

$$\text{NASA dry: } \mu_s = 0.39\exp(-0.015V_g^{0.5})\arctan(0.33\beta_g) \tag{19}$$

$$\text{NASA damp: } \mu_s = 0.25\exp(-0.042V^{0.75})\arctan(1.74\beta_g) \tag{20}$$

$$\text{NASA flooded: } \mu_s = 0.29\exp(-0.0071V^{1.25})\arctan(0.68\beta_g) \tag{21}$$

In Fig. 3, the tabular data are compared with the model. In the flooded as well as the damp condition, the increase in $\mu_s$ with slip angle is erratic. At low velocity, the friction increases (slightly) with slip angle, whereas at high velocity, the increase is (slightly) lower.

The NASA paper was based on a concrete runway. It is a well known fact to most pilots that concrete wet runways are more slippery than, for example, asphalt runways. To simulate different runways, a fourth model is added with a variable runway friction coefficient, which is independent of speed. The slip angle dependency used is similar to that for the dry NASA model. This slip angle dependency

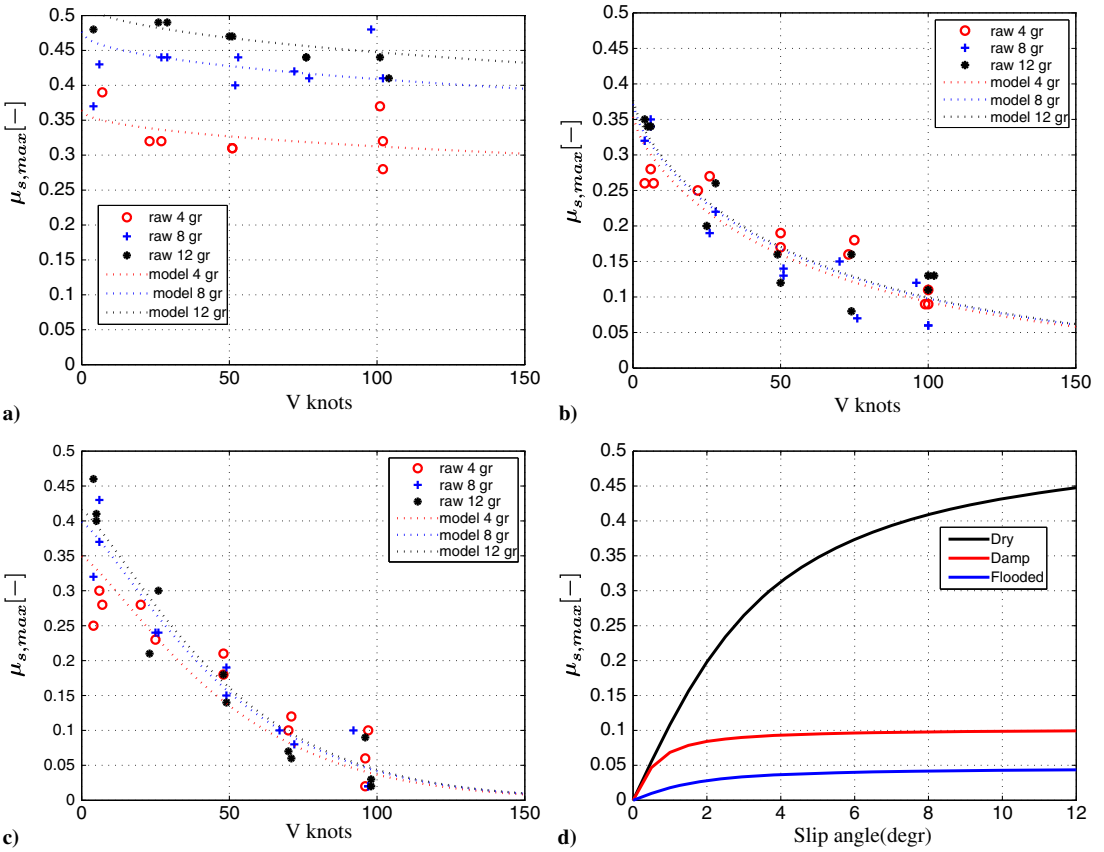


**Fig. 3 Comparison of the model used with the data of NASA [1]: a) dry runway, b) damp runway, c) flooded runway, and d) the three models compared at 100 kt.**

was chosen because the $\mu_s$ graphs for wet and flooded runways already flat out at low slip angles (see Fig. 3d), and it is expected that runways with a better texture might still show an $\mu_s$ increase at the higher slip angles:

$$\mu_s = \mu_{rwy}(2/\pi)\arctan(0.33\beta_g) \tag{22}$$

In this model, the velocity dependency is removed, but the runway friction and slip angle can be changed. This model can be used if there is a lack of adequate data that present $\mu_s$ for a nonconcrete runway as a function of slip angle, runway surface condition, and aircraft speed. However, this model is only suited to quantitatively investigate the effect of changing $\mu_s$ on the lateral deviation, but we lack the data to link this $\mu_s$ to different runway structures or different types of runway contamination.

A limitation of the NASA paper [1] is that $\mu_s$ is defined perpendicular to $V_g$, whereas for our simulation, we need the force perpendicular to $u$. If the report had also given the rolling friction in the $V_g$ direction, which most likely is higher than the normal rolling friction due to the slip angle, we could have transformed these forces to the body axes. The corrected $\mu_s$ is then $\mu_{s,\text{corr}} = \mu_s \cos(\beta_g) + \mu_{\text{roll}} \sin(\beta_g)$. As can be seen in Fig. 4, the $\sin(\beta_g)$ component is always a positive contribution to $\mu_{s,\text{corr}}$ for both positive and negative slip angles. We estimate that addition of the rolling friction component compensates at least for the reduction of $\mu_s$ due to taking the cosine. Therefore, we use the uncorrected $\mu_s$ value to calculate the side force in the body frame.

### G. Rudder Control Submodel

To simulate a continued or rejected takeoff after an engine failure, we need to design a controller that represents pilot behavior. Because pilot behavior is situation-dependent, the control laws change during the maneuver, and we have distinguished four phases. The first phase is the initial acceleration with both engines operative. The second phase is the "reaction time" phase that starts when the right engine fails; during this period, the rudder input is not changed, and the phase ends when the modeled reaction time has expired. In the third phase, maximum rudder is applied until the lateral deviation starts to decrease. In the fourth phase, the aircraft is steered back to the centerline. The steering mode has two options: with and without nose wheel steering.

A special rudder controller is only needed in phases 1 and 4, where the rudder input depends on the aircraft behavior. This rudder controller consists of three parallel inputs. The first input is based on the required rudder (and nose wheel steering) to cancel all existing moments, or

$$\delta_{\text{req}} = ((M_{z,\text{aero}} + M_{z,\text{mw}} + M_{z,\text{nw}})/(q * S * b))/(C_{n_\delta} + C_{n_{\text{nws}}}) \tag{23}$$

To calculate the nondimensional nose wheel steering coefficient $C_{n_{\text{nws}}}$, a numeric differentiation of the nose wheel moment with respect to $\delta_r$ is made. The calculated required rudder was, for stability reasons, passed through a low-pass filter with a time constant of 0.1 s.

**Table 3 Rudder controller gains**

| Mode | Proportional gain | Range, % | Rate gain | Range, % |
|---|---|---|---|---|
| NWS off | 0.15 | 25 | 2.0 | 25 |
| NWS engaged | 0.25 | 25 | 2.0 | 25 |

The second and third inputs to the controller are standard proportional and rate controllers. The gains of these controllers were experimentally tuned at different runway conditions and speeds. The proportional controller aims to steer the aircraft back to a point on the centerline 3 s in front of the aircraft but not closer than 50 m ahead. The third input is a standard rate controller. The gains and range of both the proportional and rate controller are given in Table 3. The table gives the gain values for 110 kt. For different speeds, the gains are multiplied by a speed-dependent factor $(110/V_g)^2$, which is given a maximum limit of 2.

### H. Modeling Time Delays and Lags

In an actual $V_{\text{mcg}}$ situation, there are three different variables that influence the reaction time. The first component of the reaction time is the thrust decay time, the second is the pure delay in the pilot's reaction, and the third component is the time lag required to achieve full rudder deflection.

During $V_{\text{mcg}}$ certification, the engine fuel flow is stopped abruptly; however, the thrust needs some time to decay. Based on data in [7], a linear thrust decay of 0.6 s is assumed during an engine failure. The thrust decay in a rejected takeoff of the nonfailed engine will be larger, although exact data on the thrust decay were not available. For our simulations, we estimated that the thrust would decay linearly to zero in 1 s.

Investigating these delays and lags, we found that they could be interchanged to obtain the same maneuver. For example, combining a linear rudder rate of 1 rad/s with a pilot reaction delay of 0.6 s and an engine thrust decay in 0.6 s gives a lateral deviation of 30.7 ft when the engine fails at 111 kt on a NASA dry runway. But a similar result can be achieved by using a pilot reaction time of 0.4 s and a 0.2 s decay time for engine thrust. And this similarity is not restricted to the lateral deviation; Fig. 5 shows there is a similar dynamic response in the slip angle.

A similar response was also possible by changing the pilot reaction time of 0.75 s and increasing the rudder rate to 2 rad/s. Thus, although we are faced with some unknowns in the exact rudder response and thrust decay, we can set these to realistic values and only change the pilot reaction time in our simulations. This implies that the relative effect of pilot response time can be investigated, but there might be a fixed bias depending on the actual thrust decay time and rudder response. For the remainder of the simulations, we used a linear rudder rate of 1 rad/s and a linear thrust decay of 0.6 s. With these realistic settings and a pilot reaction time of 0.5 s based on [7], our simulation very closely approaches the $V_{\text{mcg}}$ results: a 29.3 ft lateral deviation at 107 kt. Simulation also shows that the lateral

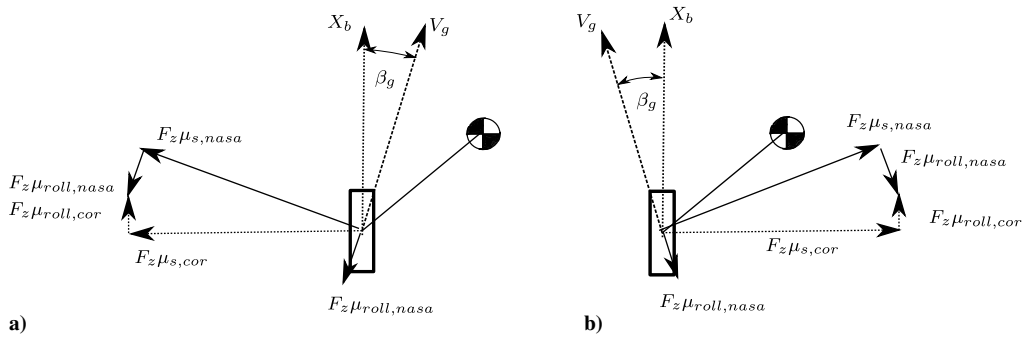


**Fig. 4 The measured $\mu_s$ in [1] is perpendicular to $V_g$. The corrected $\mu_s$ for both positive $\beta_g$ (Fig. 4a) and negative $\beta_g$ (Fig. 4b) consist of the $\mu_{s,\text{nasa}} \cos(\beta_g)$ plus an unknown contribution $\mu_{\text{roll,nasa}} \sin(\beta_g)$.**

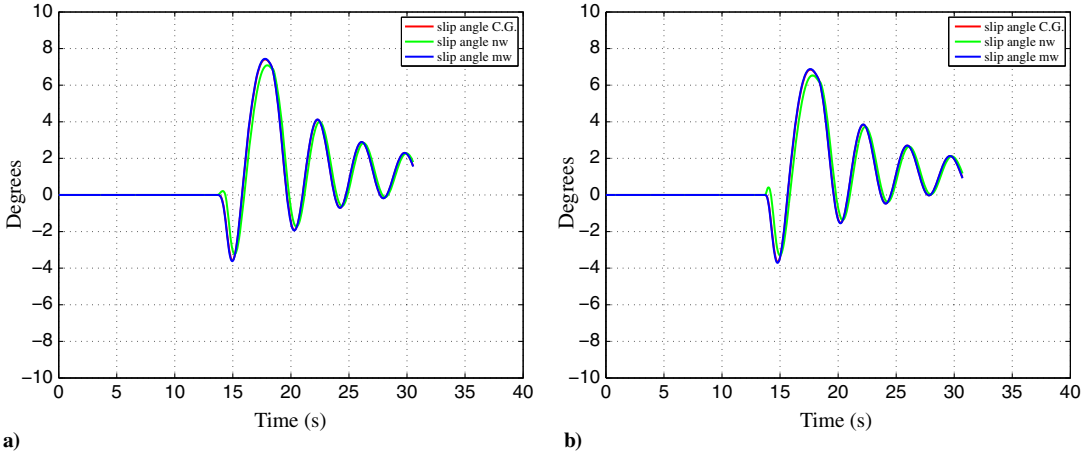


**Fig. 5 Slip after right engine failure at 111 kt on a dry runway: a) pilot reaction 0.6 s, engine devay time 0.6 s; b) pilot reaction 0.4 s, engine decay 0.2 s.**

deviation at this speed is very sensitive to changes in time delay; an increase of 0.1 s increases the lateral deviation by 8.4 ft.

## III. Basic Model Verification

We verified the model by comparing the model results with the $V_{\text{mcg}}$ certification data. In this verification case, the right engine is failed at the certified $V_{\text{mcg}}$ of 107 kt on a dry runway, under International Standard Atmosphere (ISA) and sea-level conditions with low aircraft weight and an aft c.g. located at 28% MAC. For this evaluation, we used a pilot reaction time of 0.5 s [7].

The simulation of the $V_{\text{mcg}}$ case is depicted in Fig. 6. The runway model used was the NASA model for a dry runway [Eq. (19)]. The lateral deviation is 29.3 ft, which is close to the 30 ft limit for $V_{\text{mcg}}$.

In Fig. 7, the moment and forces are displayed. It is interesting to note that the amplitude difference between aerodynamic side force

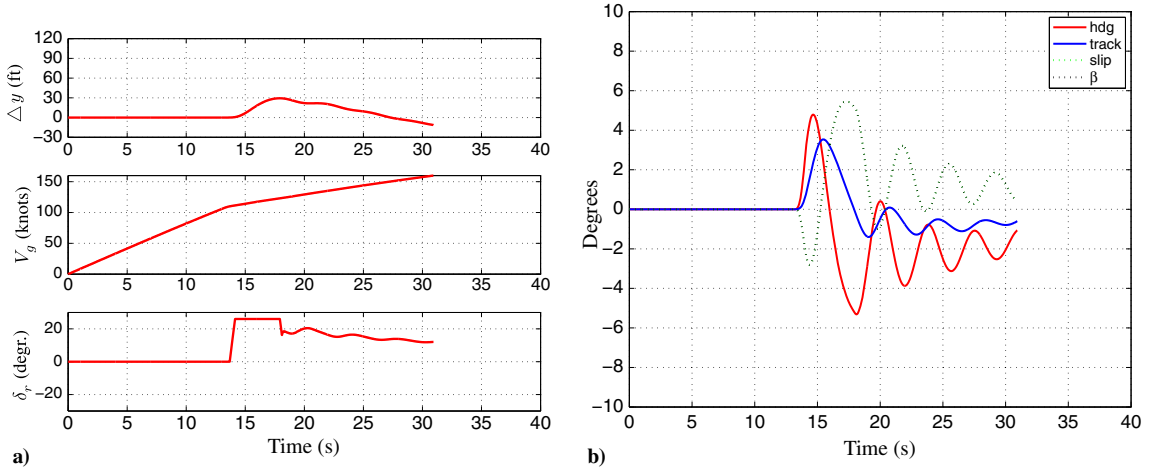


**Fig. 6 Simulation of the $V_{\text{mcg}}$ condition, a right engine failure at 107 kt, without the use of nose wheel steering and without crosswind using the NASA friction model for a dry runway.**

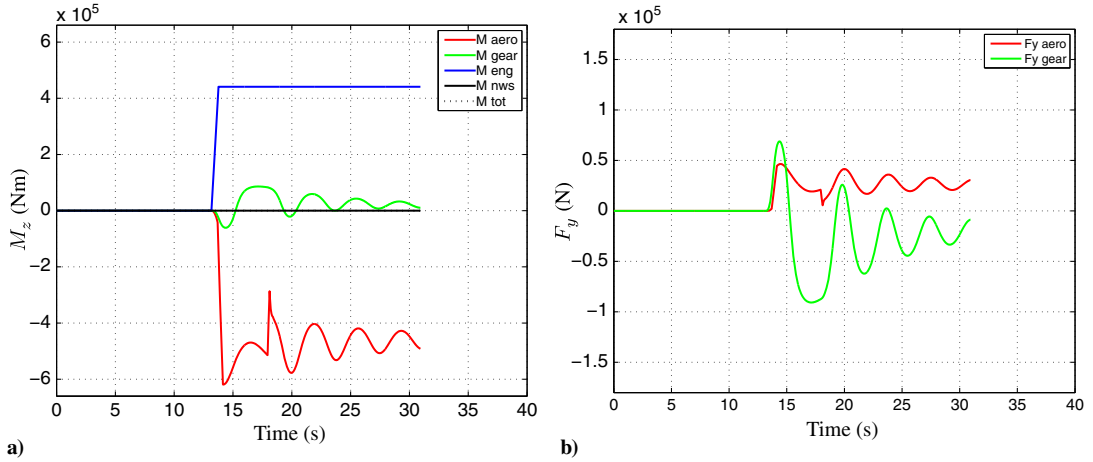


**Fig. 7 Simulation of the $V_{\text{mcg}}$ condition, a) moments around the top axis, and b) side force.**

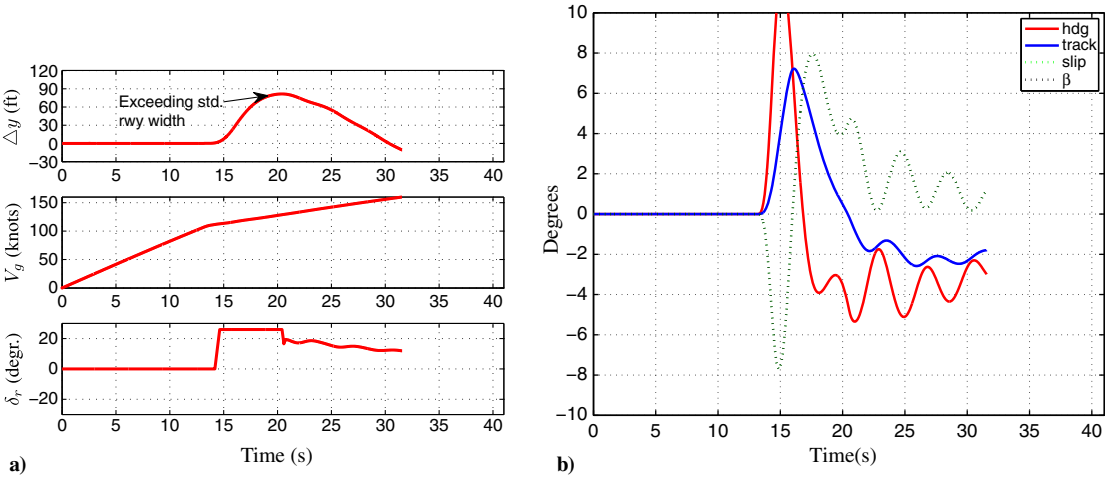


**Fig. 8 Effect of increased pilot reaction time to 1 s. Right engine failure at 107 kt, without the use of nose wheel steering and without crosswind using the NASA friction model for a dry runway.**

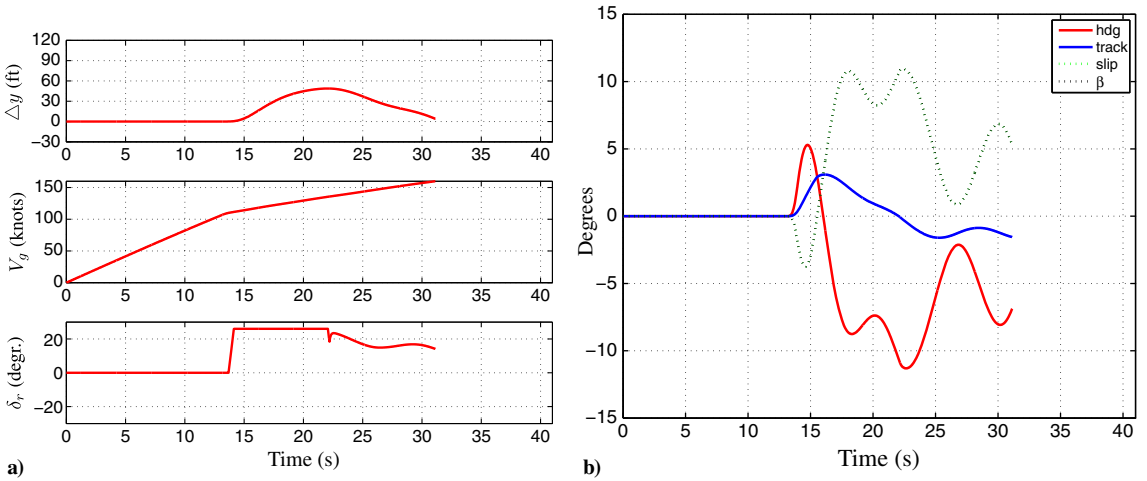


**Fig. 9 Right engine failure at 107 kt, without nose wheel steering and without crosswind using the NASA friction model for damp runway: a) trajectory, rudder, and velocity; and b) angles.**



and the side force generated by the gear is much smaller than the difference in their respective moments. This is a direct result of the small arm of the main gear in relation to the c.g. and the fact that the free castering nose wheel is not contributing to the gear moment.

## IV. Simulation Results

In this section, we evaluate the effect of time delays, runway friction, and crosswind on the lateral deviation. Our model is completely symmetric and does not have a critical engine; therefore, it is not important which engine fails, and in our simulation, it is always the right engine. We have restricted our simulations to sea-level standard day atmospheric conditions. Consequently, True Airspeed (TAS) is equivalent to Equivalent Airspeed (EAS) and the difference with Calibrated Airspeed (CAS) is negligible. However, when operating from high and hot runways, the aerodynamic forces will be similar at the same CAS, but the gear forces and moments will be lower due to the increased ground speed. On the other hand, available engine thrust might be reduced as well. For this paper, we consider the evaluation of these effects out of scope.

### A. Effect of Reaction Time

The pilot reaction time was increased to 1 s. This simulation is depicted in Fig. 8. Figure 8a shows that the lateral deviation more than doubles compared to Fig. 6a and exceeds standard runway width, a clear indication of the strong dependence of the lateral deviation on the reaction time. Figure 8b shows the increase in the associated heading, slip, and track angles due to the increased time delay.

### B. Effect of Runway Surface Condition

Figure 9 shows the effect of changing the runway friction to "NASA damp". The initial heading change is similar to the $V_{mcg}$ case; however, because of the reduced friction at this velocity, the slip angles and the track changes are now much larger.

### C. Effect of Crosswind

In our simulations, crosswind is always from the right side because this requires the maximum amount of left rudder to counteract both the weather cock effect of the crosswind and the moment of the left engine. This effect of reduced rudder control is larger than the positive effect of the side force due to sideslip and is therefore the worst-case scenario.** With crosswind, centerline control at low airspeed is not possible without nose wheel steering; therefore, the nose wheel steering is always used below 50 kt in crosswind conditions. This is also noticeable in Fig. 10a; at 50 kt, the nose wheel steering is disengaged, and the required rudder increases.

In the simulation of a crosswind condition, the aircraft will not be exactly on the centerline during the acceleration. To be able to compare different runs accurately, the lateral deviation and track error at engine fail time were corrected for. Typically, those corrections are

**This is also confirmed by simulations with crosswind from the left.

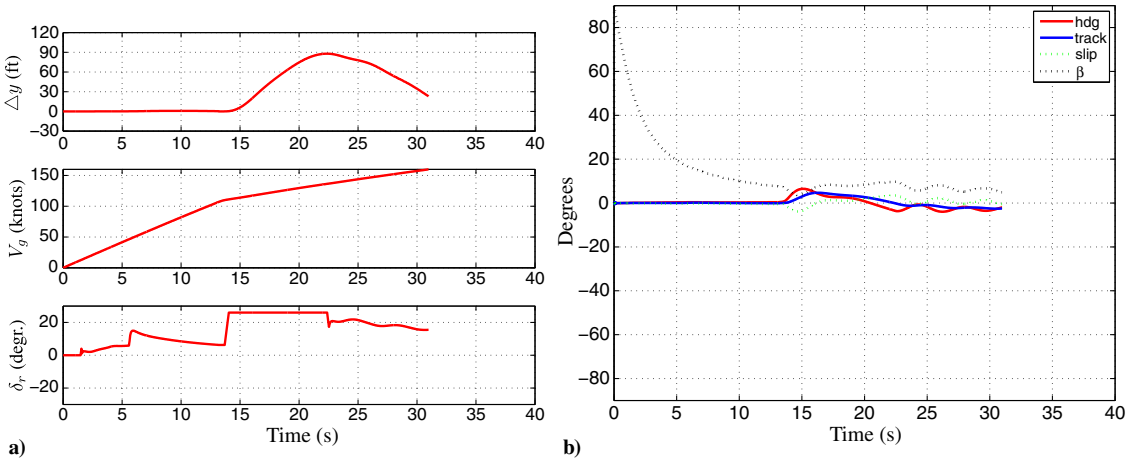


**Fig. 10 Right engine failure at 107 kt with 15 kt right crosswind, without nose wheel steering, using the NASA dry friction model: a) trajectory, rudder, and velocity; and b) angles.**

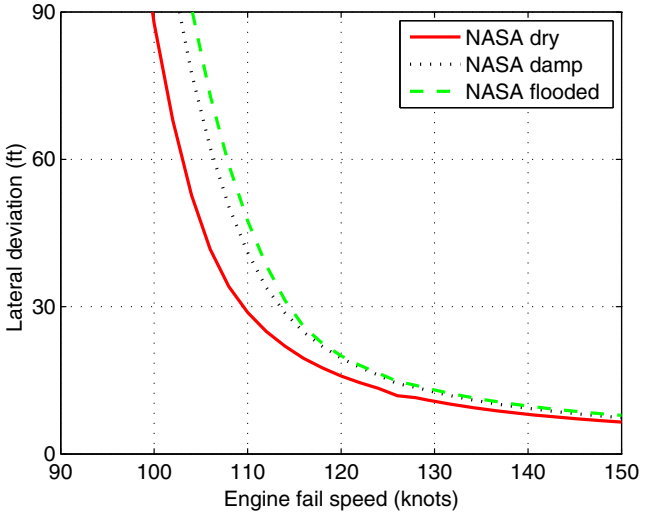


**Fig. 11 Lateral deviation as a function of engine fail speed in a 5 kt crosswind condition for three different runway surface conditions.**

less than 1 ft lateral deviation and 1 deg for heading. Also, $r$ at engine fail time was reset to zero. It is important that the deviations at engine fail time are small, otherwise the lateral deviation calculation is started with the wrong slip angle. With the applied control settings, this was achieved.

Figure 10 shows the effect of 15 kt crosswind. It is interesting to see that one third of the available rudder deflection is already used to keep the aircraft on the centerline at 111 kt; consequently, less rudder is available to counter the asymmetric engine moment. The lateral deviation increases to 88 ft, exceeding the lateral dimensions of many runways.

### D. Mixed Scenario

To show the effect of crosswind and runway surface condition, a different type of graph is used, as shown in Fig. 11. In this graph, the engine failure speed is on the $X$ axis, and the maximum lateral deviation is on the $Y$ axis. For a number of engine failure speeds, the lateral deviation has been calculated and presented for the three runway surface conditions at a given crosswind. In this way, the effect of runway surface condition is clearly shown as well as how much the engine failure speed has to be increased to obtain the regulatory 30 ft lateral deviation.

These types of plots will be used in [2], where the simulation results are used to evaluate operational procedures.

## V. Model Sensitivity

We have strived to find the most accurate values for the parameters for the Boeing 737-300. However, because it was based on Datcom plus and on the published $V_{\text{mca}}$ values, some parameters might be less accurate. Therefore, we investigated how sensitive our findings are to the accuracy of the parameters. In Table 4, the results are presented. In this analysis, parameters were changed one at a time, and thereafter the engine fail velocity that would give a 30 ft lateral deviation was determined. We will name this velocity $V_{30\,\text{ft}}$. Next, we investigated the effect of 20 kt crosswind and a change to the NASA damp runway. The standard configuration used is the lowest weight with the most aft c.g. under ISA sea-level conditions.

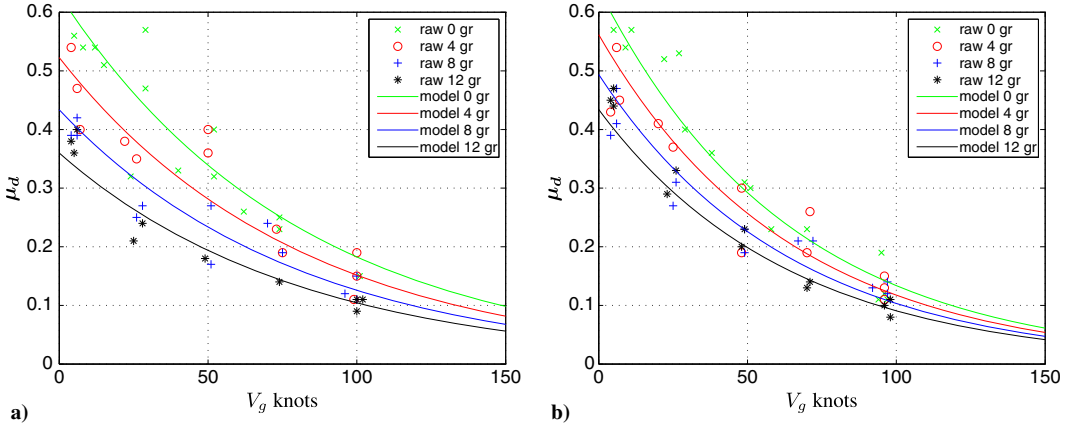


**Fig. 12 Models and raw data for a) NASA damp runway surface condition, and b) NASA flooded runway surface condition.**

**Table 4 Investigation of parameter sensitivity**

| Parameter | Change, % | $V_{30\,\mathrm{ft}}$ | Runway NASA dry to damp $\Delta V_{30\,\mathrm{ft}}$, kt | Crosswind 20 kt $\Delta V_{30\,\mathrm{ft}}$, kt |
|---|---|---|---|---|
| Standard | — — | 106.7 | 6.1 | 11.7 |
| Heavy | — — | 104.6 | 5.6 | 13.6 |
| $I_{zz}$ | +50 | 107.2 | 7.3 | 12.0 |
| $I_{zz}$ | −50 | 105.4 | 5.8 | 12.3 |
| $C_L$ | +50 | 107.5 | 5.6 | 10.6 |
| $C_L$ | −50 | 106.2 | 6.33 | 12.6 |
| $C_{Y_\beta}$ | +50 | 106.6 | 3.5 | 8.39 |
| $C_{Y_\beta}$ | −50 | 106.9 | 25.6 | 16.8 |
| $C_{Y_{\delta r}}$ | +50 | 112.6 | 19.0 | 12.4 |
| $C_{Y_{\delta r}}$ | −50 | 102.5 | 0.704 | 10.9 |
| $C_{n_\beta}$ | +50 | 105.8 | 14.1 | 25.4 |
| $C_{n_\beta}$ | −50 | 108.4 | 4.44 | 1.33 |
| $C_{n_{\delta r}}$ | +25 | 93.16 | 3.6 | 8.54 |
| $C_{n_{\delta r}}$ | −25 | 129.3 | 14.1 | 15.2 |
| $C_{n_r}$ | +50 | 106.0 | 7.27 | 12.3 |
| $C_{n_r}$ | −50 | 107.7 | 4.8 | 11.0 |
| $C_{l_r}$ | +50 | 106.7 | 6.1 | 11.7 |
| $C_{l_r}$ | −50 | 106.7 | 6.1 | 11.7 |
| $C_{l_\beta}$ | +50 | 106.7 | 6.0 | 11.6 |
| $C_{l_\beta}$ | −50 | 106.7 | 6.1 | 11.8 |
| $C_{l_{\delta r}}$ | +50 | 106.9 | 6.1 | 11.8 |
| $C_{l_{\delta r}}$ | −50 | 106.5 | 6.1 | 11.7 |
| $C_m$ | +0.2 | 106.3 | 6.2 | 12.0 |
| $C_m$ | −0.2 | 106.9 | 5.9 | 11.3 |

The third column in Table 4 shows $V_{30\,\mathrm{ft}}$ when the configuration is changed in weight and c.g. or for a change in aerodynamic parameter value. The most favorable configuration is the heaviest aircraft with the most forward c.g.; this gives a mass of 57 tons and a c.g. at 13% MAC. This configuration will give a load on the nose wheel of 0.12 mg. As can be seen in Table 4, the effect of the most favorable mass and c.g. gives a 2.1 kt lower $V_{30\,\mathrm{ft}}$.

$C_m$ was assumed to be zero; in our analysis, we investigated $C_m$ values of +0.2 and −0.2. The analysis shows that the influence of $C_m$ is very small.

The aerodynamic coefficient with the largest influence on actual $V_{30\,\mathrm{ft}}$ is, not surprisingly, $C_{n_{\delta r}}$. For this coefficient, we calculated the affect of a 25% change in parameter value; for the other coefficients, we calculated the effect of a 50% change.

Investigating the effect of model sensitivity to runway surface condition change (column 4), we see that the normal increase in $V_{30\,\mathrm{ft}}$ on a NASA damp runway is 6.1 kt. The runway surface condition effect is only very sensitive to errors in $C_{y_\beta}$, $C_{y_{\delta r}}$, $C_{n_\beta}$, and $C_{n_{\delta r}}$.

In a similar fashion, the effect of model sensitivity on crosswind (column 5) is investigated. We see that the increase in $V_{30\,\mathrm{ft}}$ for the normal configuration is 11.7 kt. This crosswind effect is only very sensitive to errors in $C_{n_\beta}$.

All these critical parameters are, not surprisingly, based on tail area and rudder power, and they are also connected. If the rudder area is decreased, both $C_{n_{\delta r}}$ and $C_{y_{\delta r}}$ will decrease, and this will influence the tail area affecting $C_{y_\beta}$ and $C_{n_\beta}$. The parameters $C_{n_{\delta r}}$ and $C_{y_{\delta r}}$ are both based on the $V_{\mathrm{mca}}$ speed, for which we assumed that $\beta$ was zero. If a small adverse $\beta$ would have been present, this would have decreased the $C_{n_{\delta r}}$ value. On the other hand, if $C_{n_{\delta r}}$ would have been significantly different, it would not have been possible to duplicate the $V_{\mathrm{mcg}}$ condition. This brings us to the conclusion that the most critical parameters in our simulation are $C_{y_\beta}$ and $C_{n_\beta}$. If these parameters are significantly larger or smaller, this will not affect the $V_{30\,\mathrm{ft}}$ speed much, but the effects of runway surface conditions and crosswind will be considerable.

## VI. Model Changes

Thus far, we have concentrated on the Boeing 737-300 model. This raises the question of how valid these findings might be for different aircraft. In this section, we evaluate this question, and the results of this evaluation are shown in Table 5. From the sensitivity analysis, we learn that the only coefficients that have a significant influence are $C_{y_\beta}$, $C_{y_{\delta r}}$, $C_{n_\beta}$, and $C_{n_{\delta r}}$. In other words, the tail area and the tail arm are the most important factors. If we change our tail area, all these coefficients are affected. On the other hand, if we change the tail arm, only $C_{y_\beta}$ and $C_{n_\beta}$ are affected. In our evaluation, we determined the new $V_{30\,\mathrm{ft}}$ for each model change and looked at the effect on the lateral deviation for different runway surface and crosswind conditions. In these simulations, the nose wheel steering was always engaged, representing the normal operational condition.

In the "big tail" simulation, all four parameters were increased by 25% and for the "small tail" decreased by 25%. As we can see in Table 5, there is a considerable and expected change of $V_{30\,\mathrm{ft}}$, but the lateral deviation effect at $V_{30\,\mathrm{ft}}$ is quite similar for the big tail simulation, whereas the lateral deviation for the small tail was considerably more for slippery runways but similar in crosswind.

In the "large arm" simulation, $C_{n_\beta}$ and $C_{y_\beta}$ were increased by 25% and decreased by 25% for the "small arm" simulation. The larger arm caused a decrease in the effect of slippery runway conditions but a larger effect of crosswind. For the small arm, these effects were reversed: an increase in the lateral deviation for slippery runways but a decrease in the effect of crosswind.

Although these effects by themselves are interesting, it is also noteworthy that, in general, the lateral deviations have the same order of magnitude, and all models show exceedances well beyond 30 ft under operational conditions. This gives us confidence that our model can be used for the evaluation of $V_{\mathrm{mcg}}$ limited V1, as is done by the authors in the second paper [2].

According to major manufacturers, a failure of the downwind engine will result in a greater lateral deviation than a failure of the upwind engine for modern aircraft with wing-mounted high-bypass engines [7]. This effect is the opposite of what we see in our model, where the weathervane effect ($C_{n_\beta}$) dominates the side force effect ($C_{Y_\beta}$). If we decrease $C_{n_\beta}$ to 20% and increase $C_{Y_\beta}$ to 150% of the original value, we duplicate the effect mentioned in [7]. The result is depicted in Table 5 in the line small $C_{n_\beta}$. The effect of crosswind from the right side (the side of the failed engine) now becomes positive, and the lateral deviation in right crosswind (from the side of the failed engine) will be lower than in no wind condition. However, crosswind from the other side becomes the most critical condition, and 25 kt crosswind will then give a 20 ft lateral displacement, but this is still much smaller than in the baseline situation. The effect of changed runway surface conditions is still present but reduced in magnitude.

## VII. Rejected Takeoff

To make our model suitable for the simulation of a rejected takeoff (RTO), two changes were required. First, the gear submodel must now include braking and account for the change in $\mu_s$, which is reduced while braking. Second, we had to change the controller. Both changes will be discussed in more detail later.

**Table 5 Investigation model changes; maximum lateral deviation at $V_{30\,\mathrm{ft}}$ with nose wheel steering engaged**

| Model change | $V_{30\,\mathrm{ft}}$ TAS, kt | NASA dry, ft | NASA damp, ft | NASA flooded, ft | 25 kt crosswind NASA dry, ft | 15 kt crosswind NASA damp, ft |
|---|---|---|---|---|---|---|
| Baseline | 106.7 | 16 | 39 | 59 | 57 | 59 |
| Big tail +25% | 94.2 | 14 | 34 | 48 | 61 | 56 |
| Small tail −25% | 125.4 | 18 | 47 | 72 | 55 | 67 |
| Large arm +25% | 92.6 | 14 | 32 | 44 | 78 | 61 |
| Small arm −25% | 129.7 | 20 | 52 | 74 | 38 | 60 |
| Small $C_{n_\beta}$ | 109.5 | 17 | 34 | 39 | 14 | 25 |

**Table 6 Brake coefficient models used**

| Runway surface condition | $a$ | $b$ | $c$ |
|---|---|---|---|
| NASA damp | 0.630 | −0.0466 | −0.0124 |
| NASA flooded | 0.647 | −0.0312 | −0.0156 |
| Variable $\mu$ | $\mu$ | −0.0466 | 0.0 |

### A. Effect of Braking on $\mu_s$

NASA [1] presents the $\mu_d$ values for different ground speeds and different slip angles, except for the NASA dry runway surface condition. For the last condition, only zero slip angle data are available. The following $\mu_d$ model was used to account for slip and ground speed:

$$\mu_d = a \exp(b\beta_g) \exp(cV_g) \tag{24}$$

where $a$, $b$, and $c$ are runway surface type dependent constants, and these constants are depicted in Table 6. For the variable $\mu_d$ option, $a$ is set to the selected $\mu_d$ value, the $b$ value is the same as for the NASA damp runway, and the velocity dependency is set to zero, as has been done for the continued takeoff scenarios presented previously. The raw data and the models are depicted in Fig. 12.

Pacejka shows in [6] (Fig. 3.13) a graphical presentation of how the side force reduces due to the presence of a braking or accelerating force. The figure shows that the vector sum of the braking force and the side force constitutes an ellipse, the largest radius gives the maximum braking force with no side force, and the smallest radius gives the maximum side force with no braking force. Unfortunately, the maximum $\mu_s$ is not known, and we cannot calculate this ellipse. However, as shown in Fig. 13a, when the braking $\mu_d$ is close to its maximum value, $\mu_s$ can be approximated by using a circle instead of an ellipse. As can be seen in Fig. 12, the reduction in $\mu_d$ due to slip angle is not more than 30%; therefore, the error using a circle approximation is limited. The maximum $\mu_d$ value for a given speed is its value at zero sideslip. The available $\mu_s$ for a given $\beta_g$ and $V_g$ is then

$$\mu_s(\beta_g, V_g) = \sqrt{(\mu_d(\beta_g = 0, V_g))^2 - (\mu_d(\beta_g, V_g))^2} \tag{25}$$

Because we now have $\mu_d$ in the $V_g$ direction and an approximated $\mu_s$ perpendicular to $V_g$, we can rotate the forces to the body axis, which was not possible for the $\mu_s$ without braking that we used in the Continued Take Off (CTO) simulation. The result for a damp runway surface condition at a $V_g$ of 50 kt is shown in Fig. 13b.

### B. Changes in Controller

The following changes were made to make the controller suitable to simulate rejected takeoffs. The first two phases of the control submodel were unchanged. In the third phase, not only was maximum rudder applied but the power of the working engine was reduced to idle. We simulated that the throttle was moved to idle at 1 s after the engine failure occurred. For the thrust reduction, we used a linear thrust decay in 1 s. Furthermore, we assumed that the spoilers would engage automatically after the throttle reduction and that the $C_D$ value increased from 0.0375 to 0.3, wheras the $C_L$ value was reduced to zero, both also in 1 s. The gain setting for the proportional gain was set at 0.35 with a 50% maximum range, whereas the rate gain was set at 0.5 with full rudder range. These settings were used with and without nose wheel steering.

There are three types of brake usage possible in phase three: 1) no brake application, 2) differential braking, and 3) symmetrical braking. When brakes are used, it is always maximum braking, and the reduced $\mu_s$ is accounted for.

One important difference in the rejected takeoff situation, when compared with the continued takeoff, was that slip angles could become excessive when runway friction was low. These large slip angles were caused by the chosen scenario in phase 3. When maximum rudder is maintained until the track moves back to the centerline, the yaw rate can have reached a very high value due to the power reduction on the nonfailed engine. This high yaw rate will than cause an excessive slip angle and a large lateral deviation to the other side of the runway. An easy way to prevent this was to reduce rudder earlier.

Several options to change the rudder control were investigated. A good option was to change from maximum rudder to the normal rudder control mode when the heading rate back to the centerline exceeded a certain value. The optimum value seems to depend on the runway surface condition and airspeed. We have used a maximum value of 4 deg/s, which worked well for most runway conditions. However, we cannot any longer claim that we calculate the minimum lateral deviation; we might call this an attainable lateral deviation, and a more sophisticated controller might be able to achieve a better result. Further optimization of the controller was considered out of scope for this paper.

## VIII. Initial Rejected Takeoff Results

An example of the RTO simulation for different braking techniques is presented in Fig. 14. The simulation shows the first lateral deviation for different right engine fail speeds on a NASA damp runway. In this simulation the rudder reaction time is set at 0.5s, reaction time for brakes is 0.2 s after full rudder application. It clearly shows the advantage of differential braking in this situation. However, in consultations with airline pilots, it became clear that it is more likely that, in a rejected takeoff, pilots would use symmetrical braking.

One of the problems with the simulation of the RTO is that the number of variables increases beyond the ones we already had for a CTO simulation. The additional variables are time delay for engine

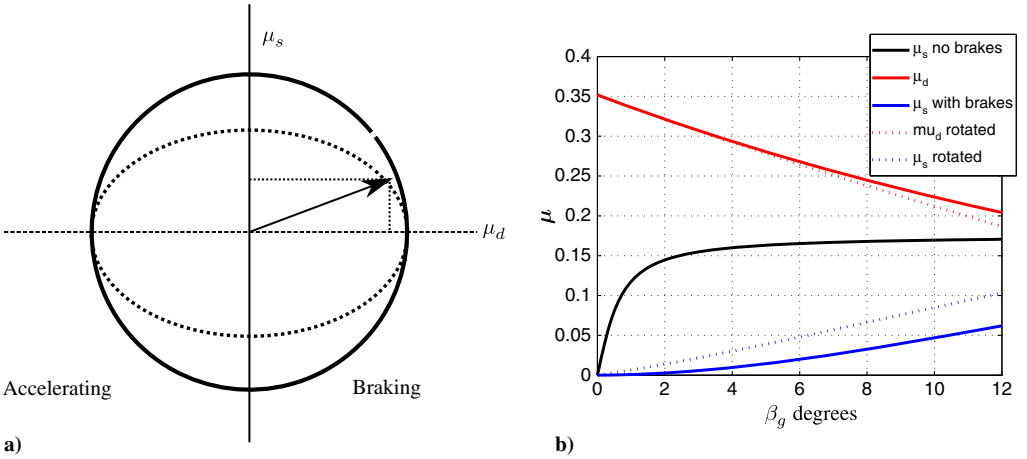


**Fig. 13 Effect of braking on available $\mu_s$: a) difference between ellipse and circle approximation for large μd values, b) $\mu_d$ and $\mu_s$ for a damp runway at 50 kt.**

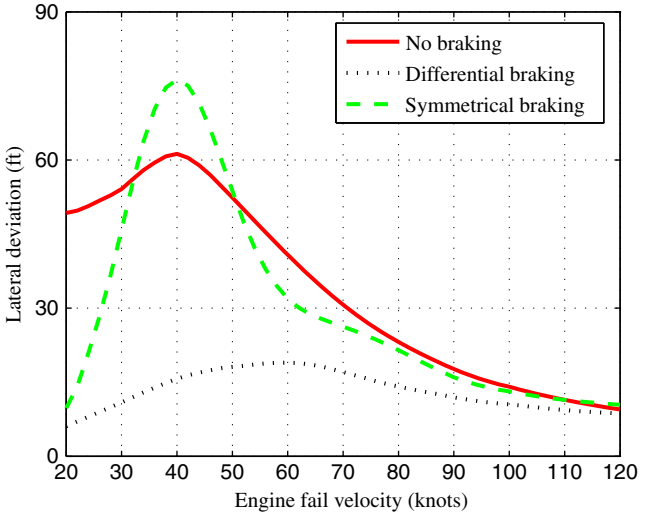


**Fig. 14 Lateral deviation in a rejected takeoff as a function of (right) engine fail speed for a NASA damp runway surface conditions with nose wheel steering engaged.**

retardation, thrust decay, time to brake application, and different brake techniques. Therefore, a full analysis of RTO is considered beyond the scope of this paper; however, this model does allow us to make some conclusions about RTO and recommendations for further research.

1) The maximum lateral deviations occur with engine failures at relative low speeds (30–60 kt), whereas the RTO at higher speed is relatively safe.

2) Simulation of the rejected take off showed that, without nose wheel steering, it was not possible to keep the aircraft on the runway at low speeds ($0 < 50$ kt) even on a dry runway.

3) Differential braking has a very positive effect on reducing the lateral deviation.

Based on these initial findings, further research to answer the following questions seems useful.

1) How well are pilots trained for low-speed RTOs and possible runway excursions at low speed?

2) How well are pilots trained in the use of differential braking?

## IX. Conclusions

By combining a generic Boeing 737-300 model, a runway surface model based on NASA test, and a tailor-made controller, a simulation model has been developed that can be used to assess the effects of runway surface conditions and crosswind on the lateral deviation for rejected as well as continued takeoff. It is believed that using the model-estimated lateral deviation for the current runway condition and crosswind for the calculation of safe $V1$ speeds can increase safety.

It would be advantageous if aircraft manufacturers, who have the most accurate aircraft data, would present the influence of runway surface condition and crosswind in a similar way.

The used NASA model has several restrictions. First, only concrete runways are considered. Second, forces are only measured in one direction, which hampers the correct rotation to the body-fixed frame. Third, the speeds are limited to 100 kt. And finally there is a large spread in the data. It would be advantageous if better models would become publicly available and integrated in flight simulators; this would enable a more realistic training of CTO and RTO in adverse conditions.

The effects on takeoff safety is addressed in a different paper [2], in which the results of this paper are used to evaluate present standards to calculate $V1$.

## Acknowledgments

This research was facilitated by Delft University of Technology, Faculty of Aerospace Engineering, Section Control and Simulation. The authors would like to thank Duke Ham, retired performance engineer of Fokker Aircraft, for sharing his expertise on this subject with us and his helpful comments.

## References

[1] Yager, T. J., and McCarty, J. L., "Friction Characteristics of Three $30 \times 11.5$–14.5, Type VIII, Aircraft Tires With Various Tread Groove Patterns and Rubber Compounds," NASA TP 1080, Dec. 1977.

[2] Huijbrechts, E., Koolstra, H. J., and Mulder, J. A., "The Use of $V_{mcg}$ as V1, Controllability Issues on Contaminated Runways and in Crosswind," *Journal of Aircraft* (to be published). doi:10.2514/1.C035222

[3] "Airplane Characteristics for Airport Planning," Boeing Document D6-58325-6, Boeing, Seal Beach CA.

[4] "Boeing 737-300 Aircraft Flight Manual," Boeing Document No. D6-8730, Boeing Company, Rento WA, 1985.

[5] Mulder, J. A., and van Staveren, W. H., *Atmospheric Flight Dynamics, (Appendix B)*, Delft Univ. of Technology, Delft, The Netherlands, Jan. 2007.

[6] Pacejka, H., *Tire and Vehicle Dynamics*, Elsevier, 2012, Chap. 3. doi:10.1016/B978-0-08-097016-5.00001-2

[7] Bolds-Moorehead, P. J., Van Chaney, G., Lutz, T. L., and Vaux, S., "Ground Minimum Control Speed Testing of Transport Aircraft," *AIAA Flight Testing Conference*, AIAA Paper 2015-3226, 2015. doi:10.2514/6.2015-3226